Chapter 1

Introduction

1.1 Introduction

Transition-metal oxides with spinel structure have drawn much attention over many years because of their intriguing physical phenomena, such as orbital ordering, geometrically frustrated magnetism, and charge ordering, due to an intricate coupling among their orbital, spin, and charge degrees of freedom. These compounds consist of a tetrahedrally coordinated *A* site and an octahedrally coordinated *B* site, as schematically shown in Fig. 1.1. The *B* sites form a network of corner-sharing tetrahedra, giving rise to the geometric frustration. The rich physics of the spinel compounds arises from various possible combinations of spin, charge, and orbital degrees of freedom of the *A*-site and *B*-site cations and their coupling to the lattice. Another interesting aspect of AV_2O_4 is that the system approaches Mott Insulator to the itinerant-electron limit with decreasing V-V separation ($R_{v\text{-}v}$).

1.1.1 Mott-Insulator

Strong interactions between electrons in a solid material can lead to surprising properties. A prime example is the Mott insulator, in which suppression of conductivity occurs as a result of interactions rather than a filled Bloch band [1].

Mott insulators are a class of materials that should conduct electricity under conventional band theories, but are insulators when measured (particularly at low temperatures). This effect is due to electron–electron interactions, which are not considered in conventional band theory. The Hubbard model offers one of the most simple ways to get insight into how the interactions between electrons can give rise to insulating, magnetic, and even novel superconducting effects in a solid. It was written down in the early 1960's and initially applied to understanding the behavior of the transition metal monoxides (FeO, NiO, CoO), compounds which are antiferromagnetic insulators, yet had been predicted to be metallic by methods which treat strong interactions less carefully. Over the intervening years, the Hubbard model has been applied to the understanding of many systems, from 'heavy fermion' systems in the 1980's, to high temperature superconductors in the 1990's. Indeed, it is an amazing feature of the model that, despite its simplicity, its exhibits behavior relevant to many of the most subtle and beautiful properties of solid state systems.

The Hubbard model has been studied by the full range of analytic techniques developed by condensed matter theorists, from simple mean field approaches to field theoretic methods employing Feynman diagrams, expansions in the degeneracy of the number of 'flavors' (spin, orbital angular momentum), etc. It has also been extensively attacked with numerical methods like diagonalization and quantum monte carlo. More formally, this model can be cast into a model Hamiltonian, the so-called Hubbard model [2]. In second quantization of quantum-field theory, the corresponding Hamiltonian is

$$\hat{H} = -t \sum_{J,l,\sigma} \widehat{\left(\partial_{J\sigma}^{\dagger}\right)} \hat{c}_{l\sigma} + \partial_{l\sigma}^{\dagger} \hat{c}_{J\sigma} + U \sum_{J} \hat{n}_{J\uparrow} \hat{n}_{J\downarrow} \tag{1.1}$$

where the operator $\partial_{j\sigma}^{\dagger}$ creates an electron in the atomic orbital $\Phi(\mathbf{r} - \mathbf{R}_j)|\sigma\rangle$. The first term is nothing but the tight-binding model of band structure (in second quantization), where t is the hopping amplitude depending on the overlap of the wavefunctions from nearest-neighbor atoms at $\mathbf{R}_1$ and $\mathbf{R}_2$

$$\mathrm{t} = \int \phi(r - R_1) \frac{e^2}{4\pi\varepsilon_{0|r-R_2|}} \phi(r - R_2)\, dr\,. \tag{1.2}$$

It describes the kinetic energy gain due to electron hopping.

The second term is the potential energy due to doubly-occupied orbitals. Here, $\hat{n}_{j\sigma} = \partial_{j\sigma}^{\dagger} \partial_{j\sigma}$ the occupation operator of the orbital $\Phi(\mathbf{r} - \mathbf{R}_j)|\sigma\rangle$ and U is the Coulomb repulsion between two electrons in this orbital,

$$U = \int \frac{e^2 |\phi(r_1 - R_j)|^2 |\phi(r_2 - R_j)|^2}{4\pi\varepsilon_0 |r_1 - r_2|}\, dr_1\, dr_2, \tag{1.3}$$

The Hubbard model is a so-called *lattice fermion model*, since only discrete lattice sites are being considered. It is the simplest way to incorporate correlations due to the Coulomb interaction since it takes into account only the strongest contribution, the on-site Coulomb interaction.

The strong-coupling limit, $U >> t$ (U is the inter-atomic Coulomb energy and t is the spin dependent expectation value for the charge transfer between sites), corresponds to materials in which valence electrons are strongly localized in their atomic orbitals (Mott-Hubbard insulator). The opposite weak-coupling limit, $U << t$, corresponds to correlated metals whose electrons are completely delocalized (Paramagnetic metal). This implies that a Mott transition is induced at a critical value Uc/t [3]. As a matter of fact, paramagnetic metals and Mott-Hubbard insulators represent two fundamentally different phases that can be interchanged by increasing or decreasing electronic correlations through a first-order quantum phase transition (QPT) [4]. It is highly challenging to characterize the electronic properties of materials when approaching the QPT either from Mott insulator side or from the paramagnetic metal side. Among very few materials, the AV_2O_4 spinels are a family of Mott insulators that fulfill the criterion of varying the t/U ratio because of the metal-metal separation can be changed by applying the chemical pressure i.e., by changing the size of the A^{2+} cation [5]. The absence of e_g electrons makes direct V-V hybridization between t_{2g} orbitals the only relevant contribution to the hopping amplitude. Moreover, t is also a function of the interionic distance, R. This volume dependence between d orbitals is $J/V^{10/3}$ [6], which is the basis of the phenomenological Bloch's equation [7] for magnetic insulators: $\alpha=\partial \ln T_N/\partial \ln V=-3.3$ provided U remains constant. When approached towards itinerant-electron behaviour the α value is very sensitive so that it can indicate the applicability of crystal-field theory.

1.1.2 Geometrically Frustration in AV_2O_4

Geometrical frustration arises when geometrical constraints promote a locally degenerate ground state. A periodic system with this local geometry may 'freeze' on cooling forming 'ices' or remain liquid down to the lowest temperatures due to quantum effects. A third possibility is that of a structural phase transition that lowers the local symmetry and lifts the degeneracy. A classic examples of geometrical frustration are the so-called pyrochlore lattice, which is also found in AV_2O_4 spinels.

1.1.3 AV_2O_4 systems

Vanadium spinel oxides AV_2O_4 (A =Fe^{2+}, Mn^{2+}, Co^{2+}, Zn^{2+}, Mg^{2+}), where A^{2+} and V^{3+} ions occupy the tetrahedral (A site) and octahedral (B site) sites, respectively, have two 3d electrons in the triply degenerate t_{2g} states at V^{3+} site. When A site is replaced by some non magnetic ion [*e.g.* Zn] it shows many interesting properties.

1.1.3.1 ZnV_2O_4

Ueda *et. al*. [8] had studied the magnetic and structural properties of $Li_xZn_{1-x}V_2O_4$ at low temperature and found that ZnV_2O_4 goes from cubic to tetragonal structure at 50 K and it goes from paramagnetic phase to antiferromagnetic phase at 40 K. The substitution of Li at Zn site suppress the structural transition and a new spin glass state appears as the ground state of Cubic phase in $0.1 < x < 0.9$ and its magnetic property study also confirmed that it's a frustrated magnetic system.

Reehuis *et. al.* [9] report on the crystallographic and magnetic structure of the geometrically frustrated spinel ZnV_2O_4 as determined by neutron powder diffraction. At T = 51 K, a cubic-to-tetragonal phase transition takes place. The low temperature crystallographic structure is characterized by the space group $I41/amd$ and unit cell dimensions $a/\sqrt{2} \times a/\sqrt{2} \times a$ with a being the lattice constant of the cubic phase. The corresponding antiferromagnetic structure of the vanadium sublattice can be described by a propagation vector **k** = (001) with the magnetic moments being aligned parallel to the *c*-axis. The ordered magneticmoment is 0.65(5) μ_B per V^{3+} ion. The experimental results are in accord with recent theoretical models proposing spin-driven Jahn-Teller distortions. The results are also compared with reports on non-ordering ZnV_2O_4 .

Lee *et. al.* [10] shows from neutron diffaraction experiment on powder sample that ZnV_2O_4 is a system of spin chains that are three-dimensionally tangled in the cubic phase above 50 K due to randomly occupied t_{2g} orbitals of V_3 ($3d^2$) ions. Below 50 K in the tetragonal phase, the chains become straight due to antiferro orbital ordering. This is

evidenced by the characteristic wave vector dependence of the magnetic structure factor that changes from symmetric to asymmetric at the cubic-to-tetragonal transition.

Ebbinghaus *et. al.*[11] have performed X-ray and Magnetic measurement on single crystal and found different behviour from polycrystalline sample. They didn't find any structural transition and antiferromagnetic transition down to 2 K. They found a spin glass behavior at 11 K which shows that single crystals are more disorder.

Zhang *et. al.* [12] studied Orbitally degenerate frustrated spinels, $Cd_{1-x}Zn_xV_2O_4$, with $0 \leq x \leq 1$ which were investigated using elastic and inelastic neutron scattering techniques. They found that with x=0 and 1, a tetragonal distortion c/a has been observed upon cooling mediated by a Jahn-Teller distortion that gives rise to orbital ordering. This leads to the formation of spin chains in the *ab*-plane that upon further cooling, Néel ordering is established due to interchain coupling. In the doped compositions, however, the bulk susceptibility, shows that the macroscopic transitions to cooperative orbital ordering and long-range antiferromagnetic ordering are suppressed. However, the inelastic neutron scattering measurements suggest that the dynamic spin correlations at low temperatures have similar one-dimensional characteristics as those observed in the pure samples. The pair density function analysis of neutron diffraction data shows that the local atomic structure does not become random with doping but rather consists of two distinct environments corresponding to ZnV_2O_4 and CdV_2O_4. This indicates that short-range orbital ordering is present which leads to the one-dimensional character of the spin correlations even in the low temperature cubic phase of the doped compositions.

Takubo *et. al.* [13] have studied the electronic structure of the spinel-type V oxides LiV_2O_4, ZnV_2O_4, and CdV_2O_4 using X-ray photoemission spectroscopy. The charge transfer energy was estimated from the valence-band photoemission spectrum. Using the transfer integrals deduced from the Harrison rule, the exchange interaction due to *d-d* transfer T_σ was found to be larger than that due to *p-d* transfer T_π, consistent with the existing theoretical models. The slight decrease of T_σ in going from the Li to Zn to Cd system would be the origin of the different magnetic properties of the three V oxides.

Specific heat and magnetic susceptibility of CdV_2O_4, ZnV_2O_4 and $MgTi_2O_4$ pellet samples have been studied over a wide temperature range by Vasiliev *et. al.* [14]. At lower temperature, both V-based spinels exhibit structural transitions followed by antiferromagnetic ordering, $T_S = 89$ K, $T_N = 30$ K in CdV_2O_4, and $T_S = 45$ K and $T_N=31$ K in ZnV_2O_4. In Ti-based spinel the complex metal–insulator-phase transformation occurs at $T_{MI} = 260$ K comprising of structural transition and a spin-singlet ground state formation.

Kuntscher *et al.* [15] have reported high-pressure resistivity and optical measurements in ZnV_2O_4 that provide unambiguous evidence of an unusual nonmonotonic behavior of the charge gap, Δ, as a function of pressure *P*. These unexpected results suggest that ZnV_2O_4 undergoes a crossover from a Mott insulator with a charge gap dominated by the on-site Coulomb repulsion *U*, to a second type of insulator in the high pressure regime.

On the other hand, when A site is replaced by Magnetic ions, different properties emerges.

1.1.3.2 MnV_2O_4

According to previous studies [16,17], MnV_2O_4 exhibits a ferrimagnetic ordering at T_N=56 K, where the magnetic moments of the Mn and the V sites align to the opposite direction, and then a structural phase transition from a cubic to a tetragonal phase at $T_s = 53$ K. Associated with this structural phase transition, the spin structure changes from a collinear Neel configuration to a noncollinear ‘‘triangular’’ structure. These results imply that the structural phase transition at 53 K is dominated by the orbital degrees of freedom on the V site, and there is an interplay between orbital and spin degrees of freedom in this compound. Polycrystalline samples of MnV_2O_4 and doped $Mn_{1-x}Zn_xV_2O_4$ and $Mn(V_{1-x}Al_x)_2O_4$ were studied by Adachi *et al.* [18] and he found that when the parent compound and $Mn_{1-x}Zn_xV_2O_4$ are compared, both T_N and T_s decrease with Zn substitution. The decrease of T_N can be explained by the decrease of the number of Mn spins. Associated with the suppression of T_N, T_s is also lowered but still exists in the Mn-site substituted samples. The size of magnetization increases with Zn doping, suggesting that the canting

angle of the triangular structure changes with Zn doping. It is to be noted that the deviation between cooling and warming runs exists far above T_s for the striction measurement of Zn-doped samples, indicating that, though a global crystal structure is cubic, a local lattice distortion is occurring even above T_s. On the other hand, the behavior of the V-site substituted samples is totally different. It has been shown that T_N does not substantially decrease, or it even increases with Al substitution for the V site. Furthermore, both the decrease of $\Delta L/L$ and the dip of M are smeared out, but they exhibit a monotonic T dependence below T_N in $Mn(V_{1-x}Al_x)_2O_4$, indicating that T_s disappears with the V-site substitution. The Al ions with no orbital degrees of freedom act as a random field on the V orbital and suppress the V orbital ordering. Such a substantial effect of a small amount of impurities indicates that the structural phase transition from a cubic to a tetragonal phase is a cooperative phenomenon dominated by orbital degrees of freedom. He also showed that with increasing magnetic field the structural transition temperature increases, which indicates a magnetic-field switching of crystal structure from a cubic to a tetragonal phase.

Garlea *et al.* [19] performed Neutron Scattering Experiment on MnV_2O_4 and found that how the existence of two consecutive magnetic transitions. The first transition is from a paramagnetic to collinear ferrimagnetic state. At a slightly lower temperature the ferrimagnetic state becomes noncollinear, with V spins developing AFM components in the ab plane. There is a simultaneously structural distortion to an orbitally ordered tetragonal phase. The appearance of an anisotropy gap indicates a strong influence of the V orbital angular momentum. They also calculated the critical exponent for MnV_2O_4 and it may be pointed out that the obtained values are close to those of the 3D Heisenberg or 3D Ising models.

Chung *et al.* [20] have measured spin wave excitations using neutron scattering and determined the effective spin Hamiltonians for MnB_2O_4 (B=V,Mn) in their noncollinear ferrimagnetic phases. In spite of the tetragonal distortions occurring in the opposite directions, the exchange interaction strength between magnetic B-site ions was always stronger in the ab plane J_{BB} than between the planes J'_{BB}. The ratio between these two constants in MnV_2O_4, $J_{BB} / J'_{BB} = 0.31$, suggests that the orbital state of MnV_2O_4 may not be explained by the simple antiferro orbital model. The microscopic spin Hamiltonian

obtained for MnV_2O_4 provides a strict test for theoretical models for the orbital physics of vanadates.

Hardy *et al.* [21] have performered magnetization, susceptibility and heat-capacity measurement on MnV_2O_4 ceramic samples. A combined analysis of magnetic and heat-capacity measurements in MnV_2O_4 clearly demonstrates that the ordering process in zero field takes place in two steps. The first transition taking place at T_N =57 K is a second order transition from paramagnetic to collinear ferrimagnetic regimes, keeping the cubic structure. It can be regarded as the standard spin ordering driven by the J_{AB} interaction in spinel oxides of general formula AB_2O_4. The second transition at lower T is a magnetostructural transtion driven by an orbital ordering at the B sites. It occurs upon warming at $T_{\uparrow s}$ = 55.5 K and upon cooling at $T_{\downarrow s}$ = 54.5 K. This ordering of the t_{2g} orbital of V^{3+} implies tetragonal distortion which in turn allows the triangular ferrimagnetic configuration to set in. Indeed, this spin ordering that is, the expected ground state in the presence of antiferromagnetic J_{AB} and J_{BB} interactions is unstable in cubic symmetry whereas it can take place in tetragonal symmetry. Upon application of magnetic field, the ferrimagnetic collinear state extents to higher temperatures large positive dT_C/dH slope, while two first order transition lines emerge from T_s. The one at higher T small positive dT_c/dH slope corresponds to the magnetostructural transition from cubic/collinear to tetragonal/triangular ferrimagnetism. Its field dependence results from a strong interplay of spin and orbital orderings. The second first order transition we observed in the phase diagram of MnV_2O_4 has a negative dT_c/dH slope. We tentatively ascribe this new line to a phenomenon of field-induced alignment within the structure of tetragonal domains. The resulting development of strains at the interfaces between domains.

Pannunzio-Miner *et al.* [22] have presented the electrical transport and magnetic susceptibility data of $Mn_{2-x}V_{x+1}O_4$ (x=0, 1/3, and 1) spinels. All the samples studied present semiconducting, positive Magneto Resistance and paramagnetic behavior associated with ferrimagnetic order at low temperature. They also found an important difference between the activation energies obtained from the Seebeck coefficient and electrical resistivity experiments. This difference is a clear indication that the predominant

conduction mechanism is by small polarons. In particular these polarons are thermally activated in the non-adiabatic regime.

Luo *et al.* [23] observed large magnetocaloric values for MnV_2O_4 system. Luo *et al.* [24] also observed large orbital entropy in Zn doped MnV_2O_4. Huang *et al.* [25] showed that doping of Fe on MnV_2O_4 increases the Magnetocaloric value of MnV_2O_4 and also it suppresses the orbital entropy value.

Kiswandhi *et al.* [26] have studied the chemical pressure effect (doping of Co on Mn site) on magnetic and transport properties of $Mn_{1-x}Co_xV_2O_4$ and also compared it with external pressure effect and found that for $Mn_{1-x}Co_xV_2O_4$, with increasing Co doping, the increasing chemical pressure (i) enhances the ferrimagnetic transition; (ii) suppresses the structural distortion; and (iii) drives the system towards the itinerant electron limit by shrinking the V-V distance. The effects on AV_2O_4 of chemical pressure are similar to the effects of physical pressure [27], confirming that the V-V distance is a critical parameter controlling the structural, magnetic, and electronic behavior of AV_2O_4 spinels.

1.1.3.3 FeV_2O_4

In FeV_2O_4 both Fe and V have orbital degree of freedom due to which it show more complex behavior compared to other vanadium spinels. According to previous studies [28], FeV_2O_4 becomes a ferrimagnetic state below $T_N = 110$ K and exhibits successive structural phase transitions at 140 K from cubic to tetragonal, 110 K from tetragonal to orthorhombic and 70 K from orthorhombic to tetragonal. In the low-temperature tetragonal phase at 70 K, the c axis is elongated and the magnetic moment is preferably oriented to that direction.

Katsufuji *et al.* [29] have also studied the structural and magnetic properties of FeV_2O_4 and found that it exhibits successive structural phase transitions from cubic, HT tetragonal, orthorhombic, LT tetragonal, to LT orthorhombic phases with decreasing temperature. They found that the tetragonal or orthorhombic domains can be aligned by the magnetic field owing to the magnetic anisotropy energy, and this induces a large magnetostriction (1%) in this compound. They also found that the magnetically easy axis is

along the ab-plane in the HT tetragonal phase, while it is along the c-axis in the LT tetragonal phase. A possible scenario for the successive structural phase transitions might be the competition and cooperation of Fe_{2p} and V_{3p} orbital's.

Nishihara *et al*. [30] have also studied the magnetic properties of FeV_2O_4 and found spin glass ordering is present in FeV_2O_4 at 85.5 K. The magnetization jumps in the M-H curves appeared below 90 K at H = 0 T. These jumps may correlate with spin-glass-like behaviors. Further, new magnetization jumps appeared below 4.6 K at H =1.2 T and these jumps are considered to be caused by spiral long range ordering with the clustering that was observed by TEM measurements.

MacDougall *et al.* [31] have performed Neutron Diffraction measurement on FeV_2O_4 and found three structural transitions as reported by other authors and reveal that the lower two transitions are associated with sequential collinear and canted ferrimagnetic transitions involving both cation sites. From local crystal and spin symmetry consideration, they further conclude that Fe^{2+} cations are ferro-orbitally ordered below 135 K and V^{3+} orbital's order at 60 K, in accordance with predictions for vanadium spinels with large trigonal distortions and strong spin-orbit coupling. Intriguingly, the direction of ordered vanadium spins at low temperature obeys "ice rules" more commonly associated with the frustrated rare-earth pyrochlore systems.

XAS, XMCD and NMR experiment on FeV_2O_4 have done by Kang *et al*. [32]. XAS experiment showed that Fe is in divalent state and V is in trivalent state. In XMCD spectra of FeV_2O_4, V2p XMCD indicates that the orbital magnetic moment for a V ion is mostly quenched due to the negligibly small spin-orbit interaction in V 3d states, and that the orbital ordering of V t_{2g} states occurs from the d_{xz} and d_{yz} real orbital states. 51-V-NMR shows that V ions are trivalent and that the canting angle θ of the V^{3+} hyperfine field is $\theta = 33^\circ \pm 2^\circ$.

Nii *et al*.[33] have performed Synchrotron XRD on FeV_2O_4 and MnV_2O_4 and conclude that the pattern of the V-OO of FeV_2O_4 was qualitatively different from that of MnV_2O_4. The V-OO in FeV_2O_4 was an F-OO with the complex orbital characterized by the

unquenched orbital angular momentum, whereas an AF-OO with real orbitals was realized in MnV_2O_4.

Zhang *et al*. [34] showed that FeV_2O_4 exhibit both ferimagnetic behavior at $T_N = 110$ K and ferroelectric behavior at $T_{N2}=56$ K. It was found that the application of a magnetic field shifts all the signatures associated to T_{N2} to higher temperatures, while it also clearly affects the value of the polarization, revealing a significant magnetoelectric coupling. They have suggested that the presence of canted spins in the triangular structure below T_{N2} could be responsible for the appearance of ferroelectricity.

Liu *et al*. [35] have studied the evolution of the structural, electric, magnetic, and multiferroic properties with x in $Fe_{1-x}V_{2-x}O_4$ ($0 < x < 0.4$) spinels. They found that increasing x form 0 to 0.3 increases the ferromagnetic transition temperature and decreases the cubic to tetragonal transition and orthorhombic to tetragonal transition temperature with ferroelectricity weakened. For $x = 0.4$, orthorhombic to tetragonal transition together with ferroelectricity disappeared. The critical composition x is around 0.3. Below x, the resistivity follows the variable range hopping model, while above x_c, the resistivity obeys nearest neighbor hopping model.

1.1.3.4 CoV_2O_4

CoV_2O_4 is also very interesting spinel vandates because it lies in the intermediate region between Mott insulator and metallic behavior. Many studies have been done on CoV_2O_4. CoV_2O_4 has been investigated since the 1960s. For example, the preparation and properties of some vanadium spinels, e.g. the doping dependence of lattice parameter, activation energy, and thermoelectric power, and the relation between V–V distance and the activation energy were reported by Rogers *et al*. [36]. The temperature dependence of magnetization and two types of transition for some spinels including CoV_2O_4 were found by Menyuk *et al.* [37]. The pressure dependence of the resistivity, lattice constant, and the corresponding activation energy for CoV_2O_4 were reported by Sawaoka *et al.* [38]. The Mossbauer emission spectra of spinel CoV_2O_4 was presented by Tejada *et al.* [39] and thus a ferrous line quadrupole split was found. The series of spinels under the assumption of the

classical Heisenberg model with only nearest-neighbor A–B, B–B interaction was investigated by Lyons *et al.* [40]. The Neel configuration with canted spin arrangement was suggested and the importance of orbital degeneracy and spin–orbit coupling in connection with the V^{3+} ions for CoV_2O_4 were found by virtue of neutron diffraction techniques in 1964 [41].

Recently Kismarahardja *et al.* [42] have studied the structure, magnetization, and resistivity under pressure on stoichiometric normal spinel CoV_2O_4 single crystals. It shows ferrimagnetic transition at 150 K. Using Arrott plot technique they calculated the critical exponent of CoV_2O_4 ($\beta = 0.24$, $\gamma = 1.80$) which does not belong from the universal class. Resistivity data under different pressure showed that for P > 6 GPA its showed metallic behavior. They have also performed the same resistivity measurement for polycrystalline sample but they did not get metallic behavior upto 8 Gpa pressure. There pressure studies on single crystals FeV_2O_4 and CoV_2O_4 clearly demonstrate that pressure and temperature do indeed effect the electronic properties strongly by changing the V-V separation. For FeV_2O_4, pressure partially delocalizes the charge carriers. For CoV_2O_4 which sits on the edge of the itinerant-electron limit, pressure actually induces metallic conductivity.

Electric, magnetic, structural, and thermal properties of spinel CoV_2O_4 have been made on polycrystalline sample by Huang *et al*. [43]. They conclude that there were paramagnetic to ferrimagnetic transition at $T_C = 142$ K and another phase transition at $T_1 = 59$ K. At 59 K and 100 K, the thermal conductivity exhibits two valleys. Below T_1, the ac magnetization shows that the phase transition leads to spin glass behavior, but the phase transition cannot be ascribed to the structural transition as revealed by the X-ray diffraction patterns.

Huang *et al*. [44] have also studied structural, magnetic and thermal properties for $Co_{1-x}Zn_xV_2O_4$ ($0.6 < x 6 < 0.2$). They found that as Zn content is increased at the Co site, the magnetic transition is suppressed. The suppression of the transition at T_1 and partial melting of the new spin-glass behavior may originate from the uplifting of the oxygen 2p bands in energy with the increase of the Zn^{2+} content.

1.2 Theoretical Background

1.2.1 Spinel Oxide

Many compounds of the AB_2O_4 family, crystallize at ambient conditions in the spinel structure. Spinel is the magnesium aluminum oxide member of this large group of materials. It has the formula $MgAl_2O_4$ and gives its name to the family of compounds that share the same structural arrangement. Consequently, here we will name as spinel to any material of general formulation AB_2O_4 which crystallizes in the cubic (isometric) crystal system with space group Fd-3m. In this structure, the O anions are located at (u, u, u), Wyckoff position 32e, with $u \approx 0.25$. They are arranged in a cubic closepacked lattice. In addition, the cations A and B occupy in the lattice respectively at tetrahedral (1/8, 1/8, 1/8) sites with Wyckoff position 8a, and octahedral (1/2, 1/2, 1/2) sites with Wyckoff position 16d. Therefore, the single positional parameter u plus the unit-cell parameter a are sufficient to determine the spinel structure. In these materials, vanadium is in the single-valence 3+ state, with electronic configuration $3d^2$. Spinel oxides can be further sub-divided into normal and inverse spinels. This can be further explained using AB_2O_4 as an example. When one type of metal cation individually occupies the tetrahedral and octahedral sites, the result is a normal spinel. On the other hand, with inverse spinels, two different types of metal cations occupy the octahedral site with only one type of cation present at the tetrahedral site. In general, the normal spinel forms when the ratio of A/B is equal to 0.5 and the inverse spinel forms when the ratio of A/B is greater than 0.5, due to possible inversion between A and B leading to the A cation occupying the octahedral sites in addition to the B cation. Spinel vanadates are the normal spinels.

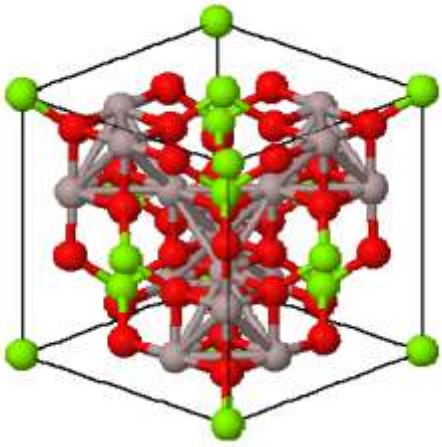

Fig. 1.1. *The idealized unit cell of spinel structure of $MgAl_2O_4$. Green site, grey site, and red site are magnesium ion, aluminum ion, and oxygen ion respectively (from reference [40]).*

In particular, this thesis work examines the physical properties in spinel vanadates. Spinel vanadates (AV_2O_4) shows ferrimagnetic behavior when A site is replaced by Magnetic ions (e.g. Mn^{2+}, Fe^{2+}, Co^{2+}) and shows antiferromagnetic behavior when A site is replaced by some non-magnetic (e.g. Zn^{2+}, Cd^{2+}, Mg^{2+}) ions. Ferrimagnets are often described as being ionic solids.

1.2.2 Crystal Field Theory

The next few sections are intended to present the fundamental concepts necessary to understand the material presented in this dissertation. To begin, we employ crystal field theory. While crystal field theory is based on an ionic model, and neglects covalent bonding character, it provides a qualitative description of transition metal oxides.

Let us consider an isolated $3d^n$ transition metal cation as shown in Fig. 1.2. The energy levels associated with its d orbitals are fivefold degenerate. When placed in a crystal field, the 3d valence electrons feel the electrostatic field created by the oxygen ligands, and the energy is raised due to the Coulombic repulsion between the valence electrons of the cation and surrounding ligands. The reduced symmetry finds that the energy of the system is lowered by lifting the fivefold degeneracy of the d orbitals and splitting them into two

energy levels: a triply degenerate level consisting of the d_{xy}, d_{yz}, and d_{xz}, orbitals and a doubly degenerate level consisting of the d_z^2 and $d_{3z^2-r^2}$ orbitals.

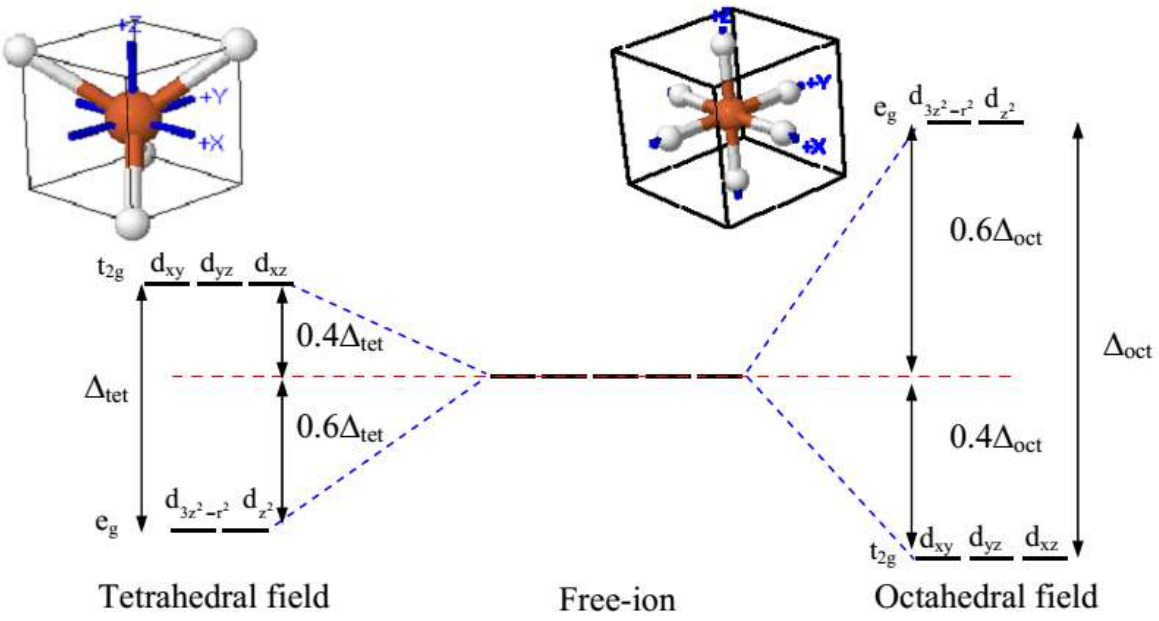

Fig 1.2. *The energy levels of the orbital in the d-electron system. The energy levels split into t_{2g} and e_g where these levels are inverted for both fields, also the energy gap in the tetrahedral field is smaller than the energy gap in the octahedral field (from reference [45])*

The symmetry of the crystal field affects the relative positions of the energy levels [46]. This can be understood for the octahedral and tetrahedral symmetries by visualizing the orientation of the d orbitals together with their oxygen ligands. In an octahedral environment, the transition metal cation is surrounded by six nearest neighbor ligands. In this coordination, Fig. 1.2 shows that the d orbitals split into lower energy t_{2g} orbitals and higher energy e_g orbitals adopting the electronic configuration $(t_{2g})^m(e_g)^n$ where m and n are integers and t_{2g} and e_g are group symmetry notation. The t_{2g} orbitals consist of the d_{xy}, d_{yz}, and d_{xz} orbitals, and the e_g orbitals consist of the d_{z^2} and $d_{x^2-y^2}$ orbitals. Representing the oxygen ligands as point charges, their spatial positions are shown in Fig. 1.3 with respect to the three coordinate axes, x, y, and z for each d orbital. The e_g orbitals point directly at the ligands where the crystal field is greatest: d_{z^2} points along the z axis, and $d_{x^2-y^2}$ points along the x and y axes. The t_{2g} orbitals, d_{xy}, d_{yz}, and d_{xz}, do not point along the coordinate axes, but rather in between them, where the field is weaker. Stronger crystal field effects

due to their atomic arrangement creates greater electrostatic repulsion between the electrons of the e_g orbitals and ligands. This raises their potential energy making them energetically less stable than the stabilized t_{2g} orbitals which have lower energy because of smaller crystal field effects.

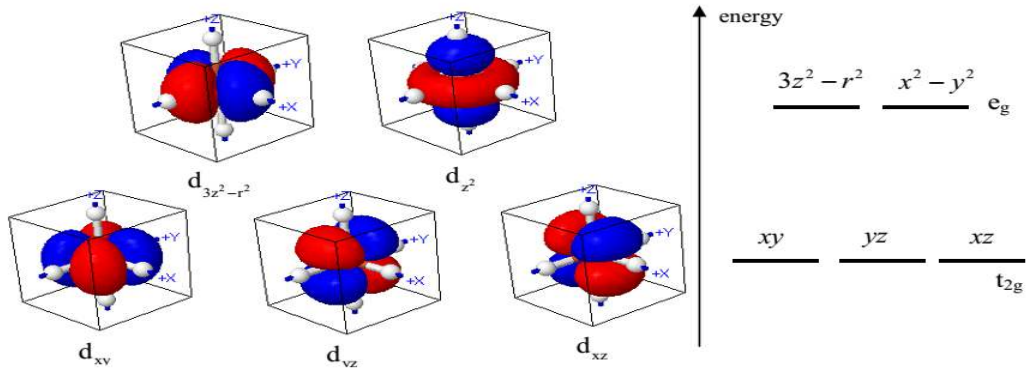

Fig. 1.3. *The orbitals of tetrahedral field, the energy levels split into triply degenerate t_{2g} and doubly degenerate e_g where the energy level of t_{2g} orbitals is higher than the energy level of e_g orbitals (from reference [45]).*

In tetrahedral symmetry, a cation is surrounded by four negative anions. The crystal field also splits the fivefold degenerate d orbitals into triply and doubly degenerate energy levels as shown in Fig. 1.3. However, the relative positions of these energy levels are reversed. The d orbitals split into lower energy e_g orbitals and higher energy t_{2g} orbitals adopting the electronic configuration $(e_g)^p(t_{2g})^q$ where p and q are integers. Fig. 1.4 shows that the t_{2g} orbitals are in closer proximity to the ligands which point towards the midpoint of the cube edges than the e_g orbitals which point towards the center of the cube faces. Similar to the discussion presented for an octahedral crystal field, the greater Coulombic repulsion between the electrons of the t_{2g} orbitals and ligands leads to their higher energy compared to the e_g orbitals. In fact, with tetrahedral symmetry no d orbital lobes point directly at a ligands.

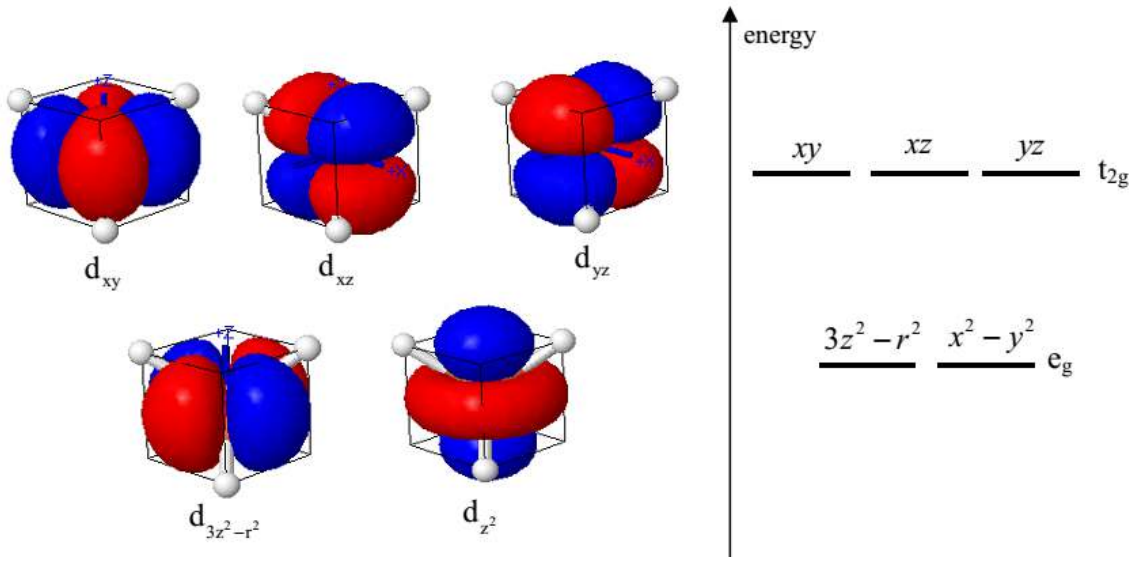

Fig. 1.4. *The orbitals of the octahedral field, the energy levels split into doubly degenerate e_g and triply degenerate t_{2g}. Unlike the tetrahedral field, the energy level of e_g orbitals in octahedral field is higher than the energy level of t_{2g} orbitals (from reference [45]).*

This is important as it provides insight regarding the energy separation between the t_{2g} and e_g orbitals with tetrahedral (octahedral) symmetry. This separation known as the crystal field splitting (Δ) varies in magnitude for octahedral (Δ_o) and tetrahedral (Δ_t) symmetry. As can be seen in Fig. 1.2, $\Delta_t < \Delta_o$ such that calculations have found a Δ_t/Δ_o ratio of 4/9 [47]. In tetrahedral symmetry, the d orbitals point in directions where the crystal field is even less than that of the octahedral t_{2g} orbitals leading to a smaller crystal field splitting.

Until this point, contributions from covalent bonding in the transition metal cation-oxygen bond has been neglected. The shortcomings of this assumption affect the crystal field splitting energy and provide an incomplete picture of the bonding. While the bond is mostly ionic, covalent bonding is present. One limitation of crystal field theory is the inaccurate prediction of the energy separation between the two orbital sets often referred to as the crystal field stabilization energy. While crystal field theory provides an estimate, covalent bonding must be considered to provide a more accurate separation energy value. For a cation with octahedral symmetry, its electronic configuration $(t_{2g})^m(e_g)^n$ is used to determine the crystal field stabilization energy from the relation $\Delta(4m\text{-}6n)/10$. For a cation

with tetrahedral symmetry, its electronic configuration $(e)^p(t_2)^q$ is used to determine the crystal field stabilization energy with $\Delta(6p-4q)/10$. However, corrections to account for covalency find that the Δ_t/Δ_o ratio changes although 4/9 remains a good approximation.

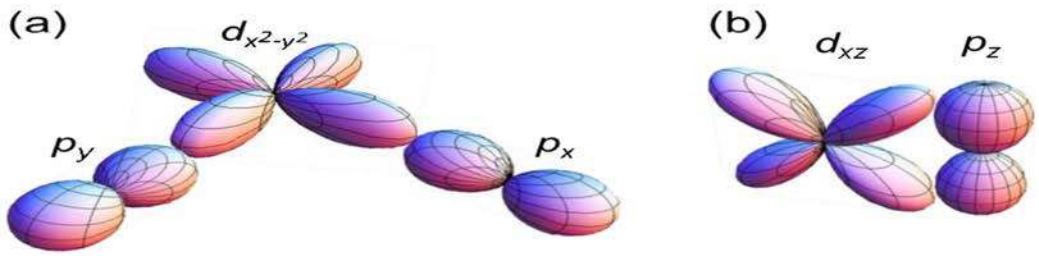

Fig. 1.5. *(a) Schematic depicting the interaction between an e_g orbital and its ligands represented by the d_x^2-$_y^2$ and p_x and p_y orbitals. The direct overlap between these orbitals indicates strong interactions and σ bonding. (b) Schematic depicting the interaction between a t_{2g} orbital and a ligand represented by the d_{xz} and p_z orbitals. The indirect overlap between these orbitals results in weaker interactions and π bonding.*

Molecular orbital theory provides a more accurate depiction of the bonding in these transition metal oxides [48]. Using a delocalized electron approach, it treats the bond between the transition metal cation and ligands as being essentially covalent and considers the role of orbital overlap. This modifies the treatment of the ligands as point charges, and instead considers the shape of the ligand bonding orbitals. As an example, I show the octahedral field as its symmetry allows for easy depiction of the overlap. Fig. 1.5(a) illustrates the strong overlap between an antibonding e_g orbital and ligands represented by the $d_{x^2-y^2}$ and the p_x and p_y orbitals. As the lobes point directly at each other, the interaction between them is greatest and indicative of σ bonding. Fig. 1.5(b) illustrates indirect overlap between an antibonding t_{2g} orbital and ligand represented by the d_{xz} and p_z orbitals. This type of overlap is indicative of π bonding.

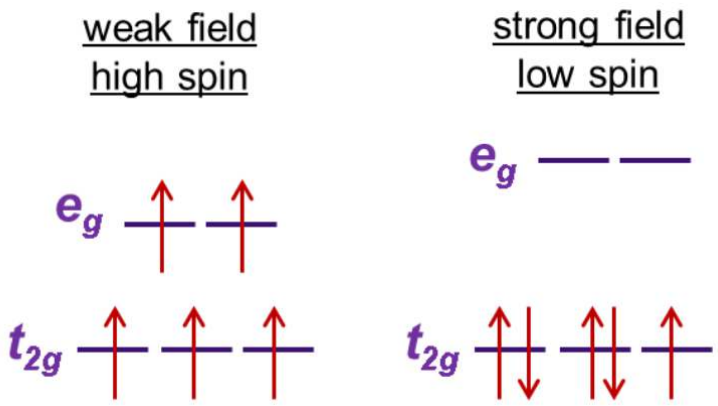

Fig. 1.6. *Schematic of the d orbital occupancy for a d^5 configuration with octahedral symmetry for the weak field and strong field cases.*

The reduced symmetry of tetrahedral fields makes such an illustration more complicated. The antibonding t_{2g} orbitals form σ bonds with its ligands. However, bonds between the antibonding e_g orbitals and their ligands are a mix of σ and π bonding since π bonding is not independent of σ bonding.

The lowest energy spin configuration becomes a competition between the crystal field energy and Hund's energy which act to keep parallel alignment between spins. For an octahedrally-coordinated cation, the order in which orbital filling occurs is unambiguous for d^1 to d^3 systems and for d^8 to d^{10} configurations. For all other systems, there is a potential for ambiguity associated with the order of orbital filling depending on the strength of the crystal field. At the extremes, as illustrated in Fig. 1.6 for a d^5 octahedral configuration, a weak field (small crystal field energy) is synonymous with a high spin state in which spin-up electrons half-fill the lower energy orbitals then jump to and begin populating the higher energy orbitals maximizing the number of unpaired electrons. For a strong field (large crystal field energy), the competition between the crystal field and Hund's energies stabilizes a low spin state as an electron would prefer to pair up with the electrons in the lower lying, half-filled energy orbitals rather than incur the energy cost of overcoming the large crystal field energy in order to populate the higher energy orbitals. In between these extremes there are systems in which the Hund's coupling and crystal field energy are closely competing and small external perturbations like temperature, pressure, and strain can push a system into high, low, or intermediate spin states. This phenomena

lies at the heart of spin state transitions research which have given rise to the discovery of new and exciting properties in complex oxides.

Finally, for tetrahedrally-coordinated cations, orbital filling is unambiguous for d^1, d^2 and d^7 to d^{10} configurations. However, as a consequence of the Δ_t/Δ_o ratio of 4/9 it is thought that the small crystal field splitting in tetrahedral complexes makes them exclusively weak field complexes [49].

1.2.3 The Jahn-Teller Theorem

1.2.3.1 Jahn-Teller Distortion

In an electronically degenerate state, a nonlinear molecule undergoes distortion to remove the degeneracy by lowering the symmetry and thus by lowering the energy [50, 51].

What is Electronically Degenerate State?

An electronically degenerate state represents the availability of more than one degenerate orbitals for an electron. In this condition the degenerate orbitals are asymmetrically occupied.

In octahedral symmetry, the d^1 configuration is said to be electronically degenerate since three t_{2g} orbitals with same energy are available for the electron to occupy. In this condition, the degenerate orbitals are also said to be asymmetrically occupied by electrons, whereas the d^3 configuration in octahedral geometry is non-degenerate and symmetric. It is not possible to put two electrons in one orbital, which is against of Hund's rule of maximum multiplicity.

In the electronically degenerate state, the orbitals are said to be asymmetrically occupied and get more energy. Therefore the system tries to get rid of this extra energy by lowering the overall symmetry of the molecule i.e., undergoing distortion, which is otherwise known as **Jahn-Teller distortion**. However considerable distortions are usually observed in **high spin d^4, low spin d^7 and d^9** configurations in the octahedral environment. It is because the Jahn-Teller distortion is usually significant for asymmetrically occupied

e_g orbitals since they are directed towards the ligands and the energy gain is considerably more.

The simple picture described above of the electronic states can be modified by lattice distortions in the form of a Jahn-Teller effect. Another facet that has given rise to interesting phenomena are structural distortions due to Jahn-Teller effects. According to the Jahn-Teller theorem, if the electronic state of a non-linear molecule is orbitally degenerate, then there is at least one vibrational coordinate along which the molecule may distort to lower its energy. Physically, this can be understood by through an example with octahedrally-coordinated Jahn Teller active $3d^9$ Cu^{2+} with a $(t_{2g})^6(e_g)^3$ ground state. If the four ligands in the xy plane move towards the Cu^{2+} ion while the two ligands along the z axis move away from the Cu^{2+} ion, then by electrostatics the d_{z^2} orbital becomes stabilized and $d_{x^2-y^2}$ is destabilized. Splitting of the lower t_{2g} orbitals also occurs accordingly. This distortion reduces the symmetry of the octahedron leaving one electron in the $d_{x^2-y^2}$orbital. Simultaneously, the distortion stabilizes the system and distortions proceed until the extra stability gained is balanced by the energy required to stretch and compress the bonds. The magnitude of the Jahn-Teller distortion depends on the bonding or antibonding power of the degenerate electrons [52]. Small splitting of the degenerate nonbonding orbitals leads to small distortions from the existing symmetry. Large distortions are expected from the increased splitting associated with removing the degeneracy of the antibonding orbitals. For octahedral sites, this occurs in the d^4 and d^9 configurations which have unpaired electrons occupying the e_g orbitals. In tetrahedral sites, unpaired electrons in the t_{2g} orbitals are expected to yield the largest distortions. This includes the d^3, d^4, d^8, and d^9 configurations.

1.2.4 Magnetism

The spinels MnV_2O_4, FeV_2O_4 and CoV_2O_4 have a magnetic ordering from paramagnetic to ferrimagnetic and antiferromagnetic for ZnV_2O_4. Different materials react differently when they are located in magnetic field. In atom, the orbital motion of the electron, the change of the orbital due to the magnetic field and the spin of the electron will affect the magnetic moment of the atom. When all electrons in the atom are paired then the magnetic spins will cancel each other so the total magnetic moments will be zero. But if there is an electron which is not paired then the atom will have a magnetic moment. In general, we can classify the magnetic property of material into several types, e.g., diamagnetic, paramagnetic, ferromagnetic, antiferromagnetic and ferrimagnetic. In diamagnetic material, all the electrons are paired or the orbital shells are filled so there is no net magnetic moment. Diamagnetic material has weak, negative magnetic susceptibility and it will be repelled in the magnetic field. In paramagnetic material, some of the atoms or ions have unpaired electrons and the orbital shells are partially filled. Paramagnetic material has small, positive magnetic susceptibility and it is slightly attracted in the magnetic field. Ferromagnetic material has strong, positive magnetic susceptibility and strongly attracted in magnetic field. In addition, ferromagnetic material will retain its magnetic properties after the magnetic field is removed. In the normal condition, without magnetic field, the magnetic domains in the ferromagnetic material are organized randomly. However, when we put a ferromagnetic material in the magnetic field, all the magnetic domains in the ferromagnetic material will eventually be parallel in the same direction. Further, when we remove the magnetic field, some domains are still pointing in the same direction. In an antiferromagnetic material, the A and B sublattice magnetic moments are equal, creating a zero net magnetic moment.

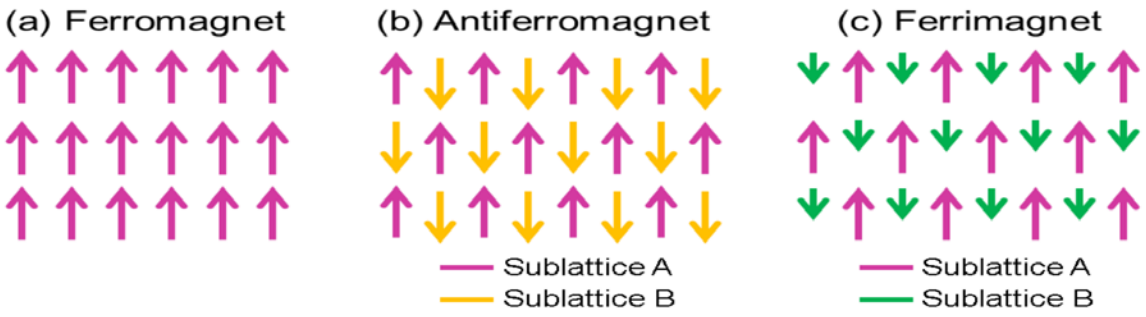

Fig. 1.7. *Long-range magnetic moment ordering for a (a) ferromagnet, (b) antiferromagnet, and (c) ferrimagnet. These magnetic classes exhibit spontaneous ordering of the moments below a critical temperature.*

Ferrimagnetism displays properties of both ferromagnetism and antiferromagnetism. Beneath a critical temperature, Fig. 1.7 shows that all three magnetic classes exhibit spontaneous long-range ordering of the magnetic moments. This ordering is the result of strong interactions between the magnetic moments attributed to the existence of a large internal molecular field, H_W. The magnetic moments in a ferromagnet exhibit parallel alignment. For antiferromagnets and ferrimagnets, nearest neighbor magnetic moments exhibit antiparallel alignment. Developed as an extension of Néel's theory of antiferromagnetism, the theory of ferrimagnetism utilizes the concept of two interpenetrating sublattices denoted as sublattice A and sublattice B. Each sublattice has its own magnetization, M_A and M_B, respectively, which is the product of the composition of each sublattice and its average magnetic moment. The total magnetization is the difference calculated by $M = |M_A| - |M_B|$. For an antiferromagnet, sublattice A and B are structurally identical such that $M_A = M_B$. This yields perfect cancellation of the magnetization and zero net moment. For a ferrimagnet, the A and B sublattices are structurally non-identical such that $M_A \neq M_B$. This results in imperfect cancellation of the magnetization and a non-zero net moment. The molecular field comes from quantum mechanics and is a construct to describe exchange interactions, but is in fact a fictitious field within a mean field approximation. Primarily electrostatic in origin and a direct consequence of the Pauli Exclusion Principle, it is concerned with the orientation of electron spins and tends to align them parallel to each other. To account for the magnetization of each sublattice requires consideration of two molecular fields as shown in equations 1.4 and 1.5 [53].

The molecular field acting on the A sublattice is

$$H_W^A = \gamma_{AA} M_A - \gamma_{AB} M_B \,, \tag{1.4}$$

The molecular field acting on sublattice B is

$$H_W^B = \gamma_{BB} M_B - \gamma_{AB} M_A \,, \tag{1.5}$$

where, γ represents the molecular field constant. For the molecular field acting on sublattice A described in equation 1.4, there are contributions from interactions between moments within the A sublattice (first term) and interactions between neighboring moments on the opposing sublattice (second term). For a ferrimagnet, the critical temperature is known as the Curie temperature (T_C). We will confined our discussion on ferrimagnetism below T_c. Above T_C, thermal agitation overwhelms the moment alignment resulting in paramagnetism. Below T_C, the magnetization for each sublattice is

$$M_A = N m_A B\left(J, \frac{\gamma_{AA} M_A - \gamma_{AB} M_B}{k_B T}\right) \tag{1.6}$$

$$M_B = N m_B B\left(J, \frac{\gamma_{BB} M_B - \gamma_{AB} M_A}{k_B T}\right) \tag{1.7}$$

where N = number of atoms/unit volume, m = magnetic moment along the field direction, B = the Brillouin function, and J = total angular momentum. The magnetization of each sublattice has its own characteristic temperature dependence. This is dependent on variables such as the cation distribution and molecular field constants. However, equations 1.6 and 1.7 also indicate that the magnetization of each sublattice is dependent on the other. This mutual dependence requires that the sublattices must have the same Curie point. Different Curie points would mean that once the magnetization of one sublattice reaches zero, it could no longer align the moments on the second sublattice thus preventing it from ordering. This is an important point for the temperature-dependent ordering of magnetic moments in ferrimagnets especially when interpreting temperature-dependent magnetic data from element-specific techniques such as X-ray magnetic circular dichroism.

Finally, as cation distribution creates a large range of structural possibilities in spinel oxide crystals, it simultaneously adds greater complexity to the observed ferrimagnetism.

The non-identical lattices require the consideration of at least three different exchange interactions: exchange between moments on sublattice A (A-A), exchange between moments on sublattice B (B-B), and exchange between moments on sublattices A and B (A-B). It is clear from the schematic in Fig. 1.7(c) that the A-B exchange is antiferromagnetic. However, there is a subtlety in the nature of the A-A and B-B exchange within each sublattice. While it appears that the exchange within each sublattice is ferromagnetic due to the observed ferromagnetic alignment, the exchange is actually antiferromagnetic. The exchange energy comes from the exchange Hamiltonian, $H_{ex} = -J_{ij}S_i \cdot S_j$. In particular we focus on the sign and magnitude of the exchange integral, J_{ij}. When $J < 0$, the exchange is antiferromagnetic. When $J > 0$, the exchange is ferromagnetic. For ferrimagnets, $J_{ij} < 0$ for all exchange interactions.

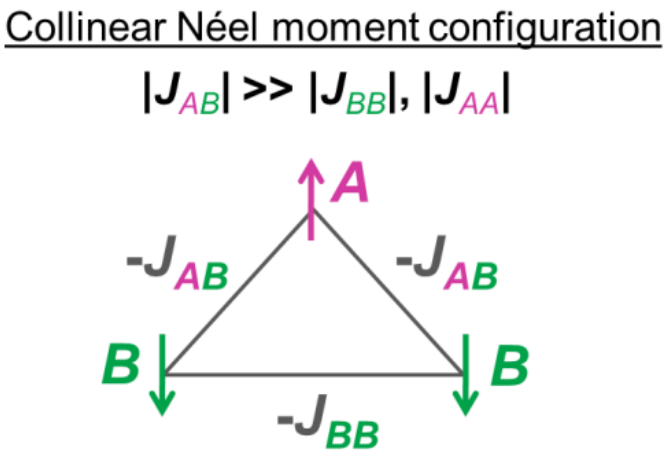

Fig. 1.8. *Spin arrangement for the three magnetic cations in a spinel formula unit under the exchange interaction conditions for the collinear Néel configuration or conventional ferrimagnet.*

For ferrimagnetic spinels, the formula unit AV_2O_4 allows for up to three magnetic cations per formula unit. The triangle-based moment geometry imposed by the crystal structure is represented by Figure 1.9. This depicts the exchange between the three magnetic cations in a collinear Néel configuration more commonly known as the conventional ferrimagnet. To achieve this configuration, the exchange condition required is $|J_{AB}| >> |J_{BB}|, |J_{AA}|$. Here the magnitude of the A-B exchange interaction is much larger than the A-A and B-B interactions. Note that the triangle-moment geometry depicts the

magnetic moments for one formula unit and as a result no A-A interactions are shown. In crystal lattices, the large proximity between the A sites results in weak exchange leading to their negligible contribution to the total exchange energy. For this reason, A-A interactions are neglected in further discussion. The ground state moment configuration is that which minimizes the overall energy of the system. Because J_{AB} is so much larger than J_{BB}, the ground state configuration is achieved by satisfying the antiferromagnetic A-B exchange term and incurring the energy cost of stabilizing parallel alignment of A-A and B-B moments. As a result, the moments between the A and B sublattice exhibit antiparallel, antiferromagnetic alignment, and the moments within the A sublattice and the moments within the B sublattice exhibit parallel, ferromagnetic-like alignment.

1.2.3.1 Frustrated Magnetism:

Within the premises of the classical Heisenberg Model, an interesting area of condensed matter physics emerges when the condition for the collinear Néel alignment does not hold, and the antiferromagnetic exchange integrals, J_{AA}, J_{AB}, and J_{BB}, are on the same order of magnitude and no longer dominated by J_{AB} [54]. A competition arises between the different exchange interactions, and the three exchange interactions cannot be simultaneously satisfied. This leads to the condition known as frustrated magnetism as the magnetic moments are unable to order and find themselves arranged in a configuration shown in Fig. 1.9.

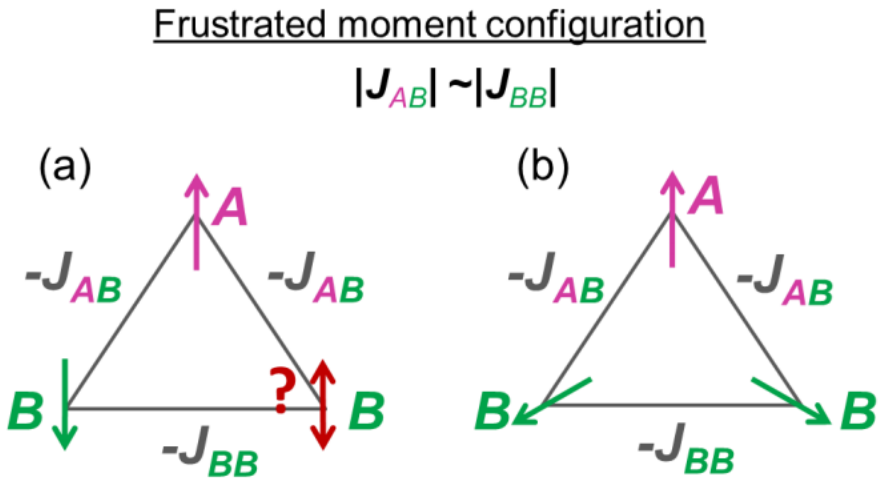

Fig. 1.9. *Spin arrangement for the three magnetic cations in a spinel formula unit under the exchange interaction conditions for frustrated magnetism. (a) Without a dominant exchange interaction, it is impossible to simultaneously satisfy all three exchange interactions as the third moment cannot order. (b) Instead the moments cant to achieve the lowest energy state possible.*

As the frustration is explained with reference to the triangle-based moment geometry, it is clear that the frustration is imposed by the crystal structure [55]. These materials are referred to as geometrically frustrated magnets. In a crystal, geometrically frustrated magnets have a large thermodynamic ground state degeneracy. Lifting this degeneracy has the potential to unlock emergent phenomena and is currently an area of active research.

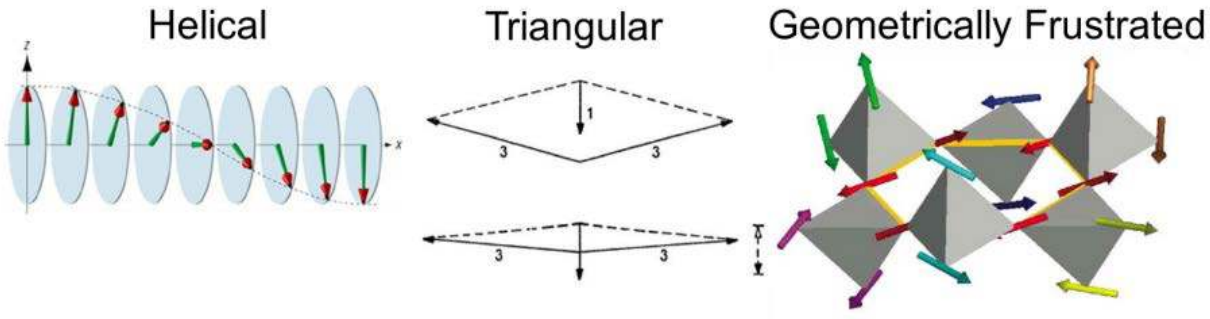

Fig. 1.10. *Examples of unusual spin configurations that arise from varying degrees of magnetic frustration [56,57].*

To qualify this statement, it is worthwhile mentioning that there are known methods for relieving some of the frustration including chemical tuning of the interstitial sites, further nearest neighbor exchange interactions, and lattice distortions. Often these mechanisms coexist leading to unusual spin configurations including helical, triangular, and monopole-like arrangements in spin ice as shown in figure 1.10. The families of spinel ACr_2O_4, chromites, and AV_2O_4 vandates are well known for exhibiting varying degrees of frustrated magnetism [58].

1.2.3.2 Superexchange

In a spinel oxide crystal, magnetic cations are second nearest neighbors because first nearest neighbors are oxygen anions. The increased proximity between magnetic cations minimizes their orbital overlap effectively weakening their direct exchange. Instead, ferrimagnetism arises from superexchange, an indirect exchange mechanism mediated by the oxygen anion and is a direct consequence of the covalent bonding term.

Superexchange can be explained from the perspective of the oxygen anion [59]. The O^{2-} ion has a filled 2p valence shell ($2s^2 2p^6$). However, the presence of neighboring transition metal cations will perturb this closed shell configuration such that a 2p electron finds itself belonging to the neighboring transition metal cations for a short period. Perturbations of this nature find that the lowest energy state for oxygen is a superposition of the O^{2-} ground state and excited O and neutral O states. Electron transfer occurs via hopping and preserves spin orientation. An electron may only hop into the neighboring orbital if its spin orientation is allowed by the Pauli Exclusion Principle and favored by Hunds rule. The other 2p electron of opposite spin may now interact with the other neighboring transition metal cation assuming the interaction is in accordance with the Pauli exclusion principle and Hund's rule. Superexchange is strongest for bond angles of 180º, and weakens as the angle becomes smaller [60]. For a spinel, the largest superexchange term originates from the approximately 125º angle formed by the A-O-B ions. There are also contributions from the 90º bond angle formed by the B-O-B ions. There are no A-O-A bonds and thus no expected superexchange. It is also noteworthy that the smaller ionic

radius of oxygen leads to the prediction of direct exchange in ionic solids for particular combinations of electronic structure with a 90º bond angle [61].

1.2.4 Magneto Caloric Effect

The magnetocaloric effect (MCE) is defined as the heating or cooling (i.e., the temperature change) of a magnetic material due to the application of a magnetic field. This effect has been called adiabatic demagnetisation for years, though this phenomenon is one practical application of the MCE in magnetic materials. The magnetocaloric effect was discovered in 1881, when Warburg observed it in iron [62]. The origin of the MCE was explained independently by Debye [63] and Giauque [64]. They also suggested the first practical use of the MCE: the adiabatic demagnetisation, used to reach temperatures lowers than that of liquid helium, which had been the lowest achievable experimental temperature.

Nowadays, there is a great deal of interest in using the MCE as an alternative technology for refrigeration, from room temperature to the temperatures of hydrogen and helium liquefaction (20-4.2 K). The magnetic refrigeration offers the prospect of an energy-efficient and environment friendly alternative to the common vapour-cycle refrigeration technology in use today [65, 66].

In order to explain the origin of the magnetocaloric effect, we use thermodynamics, which relates the magnetic variables (magnetisation and magnetic field) to entropy and temperature. All magnetic materials intrinsically show MCE, although the intensity of the effect depends on the properties of each material. The physical origin of the MCE is the coupling of the magnetic sublattice to the applied magnetic field, H, which changes the magnetic contribution to the entropy of the solid.

The equivalence to the thermodynamics of a gas is evident (Fig. 1.11): the isothermal compression of a gas (with application of pressure decrease of the entropy) is analogous to the isothermal magnetisation of a paramagnet or a soft ferromagnet (with application of magnetic field decrease of the magnetic entropy), while the subsequent adiabatic expansion of a gas (lowering of pressure at constant entropy and decrease of temperature) is equivalent to adiabatic demagnetisation (withdrawn H, the total entropy remains constant and temperature decreases as the magnetic entropy increases).

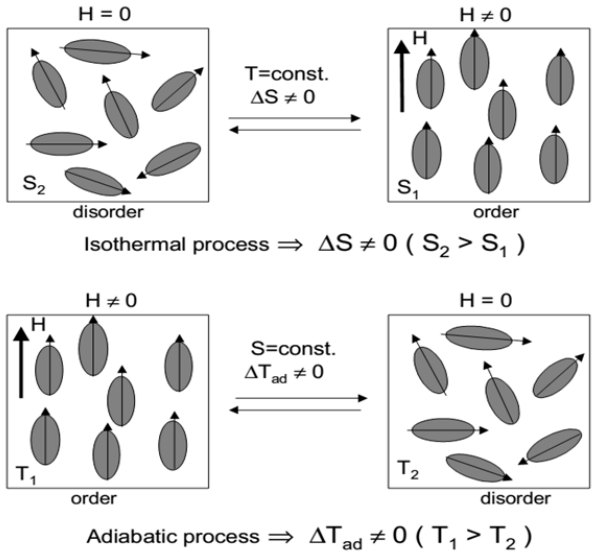

Fig. 1.11. *Schematic picture that shows the two basic processes of the magnetocaloric effect when a magnetic field is applied or removed in a magnetic system: the isothermal process, which leads to an entropy change, and the adiabatic process, which yields a variation in temperature.*

The value of the entropy of a ferromagnet (FM) at constant pressure depends on both H and temperature, T, whose contributions are the lattice (S_{lat}) and electronic (S_{el}) entropies, as for any solid, and the magnetic entropy (S_m),

$$S(T, H) = S_m(T, H) + S_{lat}(T) + S_{el}(T) \quad (1.8)$$

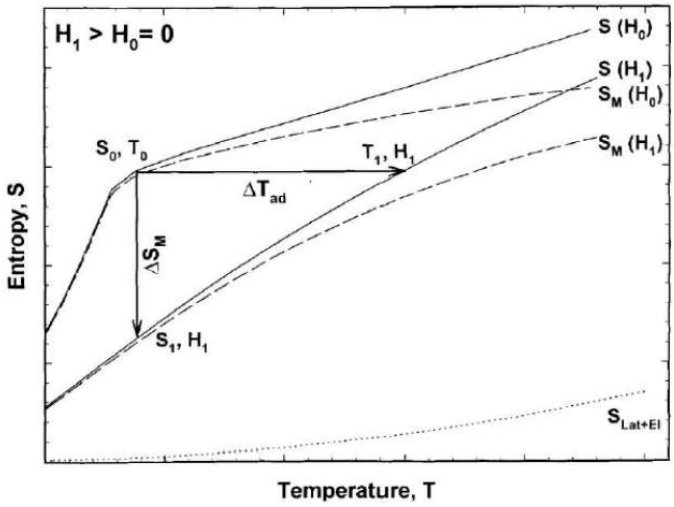

Fig. 1.12. *S-T diagram showing the MCE. Solid lines represent the total entropy in two different magnetic fields ($H_0 = 0$ and $H_1 > 0$), dotted line shows the electronic and lattice contributions to the entropy (non-magnetic), and dashed lines show the magnetic entropy in the two fields. The horizontal arrow shows ΔT_{ad} and the vertical arrow shows ΔS_m, when the magnetic field is changed from H_0 to H_1. Taken from Ref. [67].*

Fig. 1.12 shows a diagram of the entropy of a FM near its Curie temperature, T_C, as a function of T. The total entropy is displayed for an applied external field, H_1, and for zero field, H_0. The magnetic part of the entropy is also shown for each case (H_1 and H_0). Two relevant processes are shown in the diagram in order to understand the thermodynamics of the MCE:

(i) When the magnetic field is applied adiabatically (i.e., the total entropy remains constant) in a reversible process, the magnetic entropy decreases, but as the total entropy does not change, i.e.,

$$S(T_0, H_0) = S(T_1, H_1) \tag{1.9}$$

then, the temperature increases. This adiabatic temperature rise can be visualized as the isentropic difference between the corresponding S(T, H) functions and it is a measurement of the MCE in the material,

$$T_{ad} = T_1 - T_0 \tag{1.10}$$

(ii) When the magnetic field is applied isothermally (T remains constant), the total entropy decreases due to the decrease in the magnetic contribution, and therefore the entropy change in the process is defined as

$$S_m = S(T_0, H_0) - S(T_0, H_1) \tag{1.11}$$

Both the adiabatic temperature change, T_{ad}, and the isothermal magnetic entropy change, S_m, are characteristic values of the MCE. Both quantities are functions of the initial temperature, T_0, and the magnetic field variation $H = H_1 - H_0$. Therefore, it is straightforward to see that if rising the field increases magnetic order (i.e., decreases magnetic entropy), then $T_{ad}(T, H)$ is positive and magnetic solid heats up, while $S_m(T, H)$ is negative. But if the field is reduced, magnetic order decreases and $T_{ad}(T, -\Delta H)$ is thus negative, while $S_m(T, -\Delta H)$ is positive, giving rise to a cooling of the magnetic solid.

The relation between H, the magnetisation of the material, M, and T, to the MCE values, $\Delta T_{ad}(T, \Delta H)$ and $\Delta S_m(T, \Delta H)$, is given by one of the Maxwell relations[63]:

$$\left(\frac{\partial S(T,H)}{\partial H}\right)_T = \left(\frac{\partial M(T,H)}{\partial T}\right)_H, \tag{1.12}$$

Integrating Eq. 1.5 for an isothermal (and isobaric) process, we obtain

$$\Delta S_m(T, \Delta H) = \int_{H_1}^{H_2} \left(\frac{\partial M(T,H)}{\partial T}\right)_H dH \,, \tag{1.13}$$

This equation indicates that the magnetic entropy change is proportional to both the derivative of magnetisation with respect to temperature at constant field and to the field variation. Using the following thermodynamic relations [63]:

$$\left(\frac{\partial T}{\partial H}\right)_S = -\left(\frac{\partial S}{\partial H}\right)_T \left(\frac{\partial T}{\partial S}\right)_H \,, \tag{1.14}$$

$$C_H = T\left(\frac{\partial S}{\partial T}\right)_H \tag{1.15}$$

where C_H is the heat capacity at constant field, and taking into account Eq. 1.8, the infinitesimal adiabatic temperature change is given by

$$dT_{ad} = -\left(\frac{T}{C(T,H)}\right)_H \left(\frac{\partial M(T,H)}{\partial T}\right)_H \,, \tag{1.16}$$

After integrating this equation, we obtain other expression that characterizes the magnetocaloric effect,

$$\Delta T_{ad}(T, \Delta H) = -\int_{H_1}^{H_2} \left(\frac{T}{C(T,H)}\right)_H \left(\frac{\partial M(T,H)}{\partial T}\right)_H dH \,, \tag{1.17}$$

By analyzing Eqs. 1.9 and 1.13, some information about the behaviour of the MCE in solids can be gained:

1. Magnetisation at constant field in both paramagnets (PM) and simple FMs decreases with increasing temperature, i.e., $(\frac{\partial M}{\partial T})_H < 0$. Hence $\Delta T_{ad}(T, \Delta H)$ should be positive, while $\Delta S_m(T, \Delta H)$ should be negative for positive field changes, $\Delta H > 0$.

2. In FMs, the absolute value of the derivative of magnetisation with respect to temperature, $|(\frac{\partial M}{\partial T})_H|$, is maximum at T_C, and therefore $|\Delta S_m(T; \Delta H)|$ should show peak at $T = T_C$.

1.2.5 Transport Properties

1.2.5.1 Variable Range Hopping

MnV_2O_4, FeV_2O_4 and CoV_2O_4 are insulators and semiconductor. The electrical transport in these materials is thermally activated and Variable Range Hopping (VRH) model is one of the physical models that can describe the temperature dependence of the

conductivity in the insulating system. Sir Nevill Mott [64] proposed VRH model to describe the behavior of the resistivity in systems with disorder and at low temperature.

Suppose we have two states in which their distance is *r* and they are localized, if the first state has energy E_1 and the second state has energy E_2 and the energy difference $W = E_2 - E_1 > 0$ then the electron can jump from the first state to the second state by absorbing a phonon. If μ_1 and μ_2 are the electric potential energy of the first state and second state, then the current is given by

$$I = \frac{er\omega_0}{k_B T}(\mu_1 - \mu_2)exp(-W/k_B T)exp(-2r/\xi), \tag{1.18}$$

By taking μ_1-μ_2 = eV, the resistance can be evaluated as

$$R = \frac{k_B T}{e^2 r\omega_0}(exp(-W\ /\ k\_B\ T)exp(-2r/\xi)\ )^{-1} \tag{1.19}$$

where ω_0 is a frequency from typical phonon and ξ is the localization length. The conductivity can be written

$$\sigma = \sigma_0 exp\left(-\frac{2r}{\xi} - \frac{W}{k_B T}\right) \tag{1.20}$$

For d = 3, the density *N{E}* is given by

$$N\{E\} = \frac{3}{4\pi r^3 W}, \tag{1.21}$$

$$W = \frac{3}{4\pi r^3 N\{E\}}, \tag{1.22}$$

where *N{E}* is the density of states.

Putting the equation (1.22) into equation (1.20) and maximizing σ by taking its derivative = 0, we obtain

$$r = \left(\frac{9\xi}{8\pi N\{E\}k_B}\right)^{\frac{1}{4}}\left(\frac{1}{T}\right)^{\frac{1}{4}} \tag{1.23}$$

Substituting equation (1.23) into equation (1.20) and finally we obtain

$$\sigma = \sigma_0 \exp[-(T_0/T)^{0.25}] \tag{1.24}$$

which implies

$$\rho(T) = \rho_0 \exp(T_0/T)^{0.25} \tag{1.25}$$

where T_0 is the characteristic barrier energy parameter and it can be calculated from the slope of lnρ versus $(1/T)^{0.25}$ curve (Fig. 1.13 (a)). Finally, we obtain the relation between the barrier energy parameter T_0 and the localization length ξ by putting the value of r from equation (1.23) into equation (1.20) and evaluate for T_0, we obtain

$$T_0 \propto \frac{1}{N\{E\}\xi^3} \quad , \tag{1.26}$$

Localization length is a characteristic of a localized system where the smaller ξ is, the more localized the system. A physical interpretation of the localization length in a localized system is illustrated in Fig. 1.13 (b)

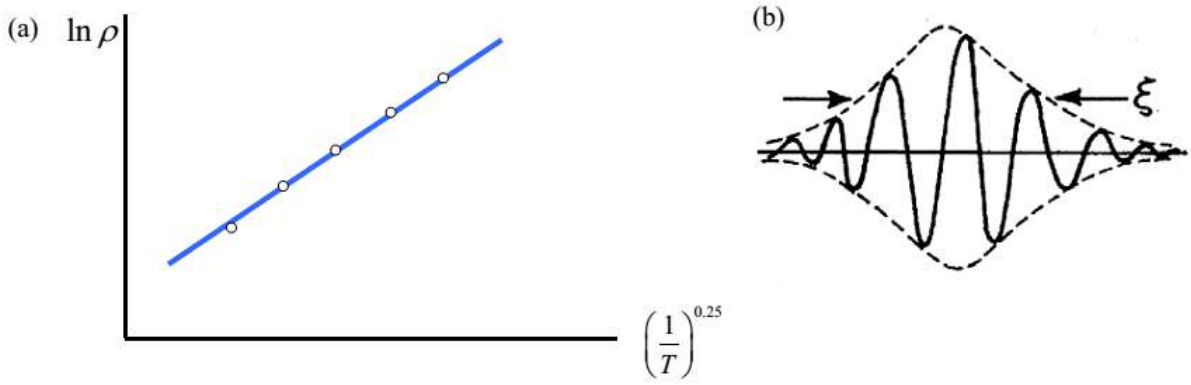

Fig. 1.13. *(a) ln ρ versus $(1/T)^{0.25}$ from VRH model, the barrier energy parameter T_0 is calculated from the slope of the curve. (b) The localization length in the localized wave function (from reference [70]).*

1.2.5.2 Arrhenius law

The discussion on Arrhenius law is also given here in order to describe the temperature dependence of the resistance of a system which its electrical transport has a thermally activated behavior. Originally, the Arrhenius equation was proposed by Dutch chemist, J.H van't Hoff in 1884. However, Svante Arrhenius was the first person who gave the physical interpretation of this equation. He was using this equation to explain the dependence of the rate constant k of a chemical reaction on the activation energy E_a and temperature T.

$$k = A \exp(-E_a / RT), \quad (1.27)$$

where R is a gas constant. In general, many thermally activated processes can be evaluated by using Arrhenius law. In the electrical transport mechanism, the resistance of a semiconducting or an insulating material can also be explained by using this model and we can express the resistance (resistivity) as following

$$R = R_0 \exp(E_a / k_B T) , \quad (1.28)$$

here, k_B is the Boltzman constant and E_a is the activation energy and can be obtained from the slope of ln ρ versus (1/ T) curve (Fig. 1.14 (a)).

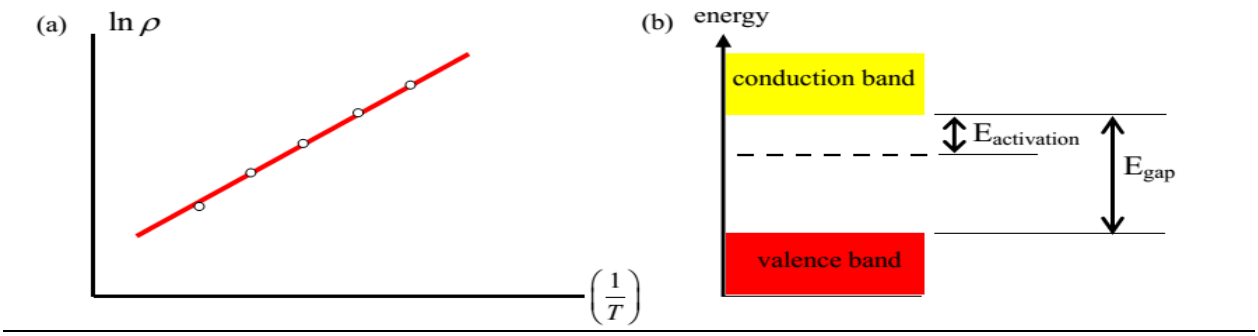

Fig. 1.14. *(a) ln ρ versus (1/T) from Arrhenius model. (b) The activation energy and the band gap between valence and conduction bands.*

1.2.6 The Modified Arrott Plot

The modified Arrott plot is a scaling technique to determine the critical exponents, e.g, β, γ and δ, and the critical temperature T_c for the ferromagnetic (and ferrimagnetic) system. The modified Arrott plot can be used in order to study the critical spin fluctuations near the ferromagnetic transition, by analyzing the spontaneous magnetization M_s and the inverse of the initial susceptibility χ_0^{-1} based on the magnetization versus field measurements near the transition temperature. Arrott plot was originated from the Landau theory of the second order ferromagnetic phase transition. According to this theory, the free energy is written as a power series of the magnetization. Before the modified Arrott plot,

there was a plot called Arrott plot proposed by A. Arrott [71]. In general, this plot is non linear and there is a difficulty to determine accurately the value of M_s, χ_0^{-1}. However, Anthony Arrott and John E. Noakes then suggested a more practical and powerful plot and is known as the modified Arrott plot [72]. In the modified Arrott plot, we plot the $M_s^{1/\beta}$ versus $(H/M)^{1/\gamma}$ from the M-H data around the transition temperature. This plot yields a set of parallel straight lines near T_c. The relations of the spontaneous magnetization M_s and the inverse of the initial susceptibility χ_0^{-1} are given by

$$(\chi_0)^{-1}(T) \propto (T - T_c)^{\gamma} \text{ , for } T > T_c \tag{1.29}$$

$$H \propto M^{\delta}, \text{ for } T = T_c \text{ and} \tag{1.30}$$

$$M_s(T) \propto (Tc - T)^{\beta} \tag{1.31}$$

From the Arrott plot, we can see if a system obeys the Ising model or Heisenberg model or the Molecular Field Theory.

Reference

[1]. Mott, N. F., Metal–Insulator Transitions, Taylor & Francis, 1990.

[2]. Fazekas, P., Lecture notes on electron correlation and magnetism, World Scientific, Singapore, 2003.

[3]. Brinkman, W. F. and Rice, T. M., Application of Gutzwiller's Variational Method to the Metal-Insulator Transition, Phys. Rev. B, 2, 4302-4304, 1970.

[4]. Goodenuogh, J. B., Structure and Bonding, springer Verlag Berlin, Vol. 98 (chapter 1 & 2) 2001.

[5]. Canosa, S. B., Rivadulla, F., Pardo, V., Baldomir, D., Zhou, J. S., García-Hernández, M., López-Quintela, M.A., Rivas, J. and Goodenough, J. B., Enhanced Pressure Dependence of Magnetic Exchange in $A^{2+}[V_2]O_4$ Spinels Approaching the Itinerant Electron Limit, Phys. Rev. Lett., 99, 187201/1-187201/4, 2007.

[6]. Harrison, W.A., Editor, in Electronic structure and the properties of solid: The Physics of the chemical bond, W. H. Freeman & co. San Francisco (1980).

[7]. Bloch, D., The 10/3 law for the volume dependence of superexchange, Journal of Physics and Chemistry of Solids, 27, 881-885, 1966.

[8]. Ueda, Y., Fujiwara, N. and Yasuoka, H., Magnetic and Structural Transitions in $(Li_xZn_{1-x})V_2O_4$ with the Spinel Structure, J. Phys. Soc. Japan, 66, 778-783, 1997.

[9]. Reehuis, M., Krimmel, A., Buttgen, N., Loidl, A. and Prokofiev, A., Crystallographic and magnetic structure of ZnV_2O_4 Structural phase transition due to spin-driven Jahn-Teller distortions, Eur. Phys. J. B, 35, 311-316, 2003.

[10]. Lee, S. H., Louca, D., Ueda, H., Park, S., Sato, T. J., Isobe, M., Ueda, Y., Rosenkranz, S., Zschack, P., Iniguez, J., Qiu, Y. and Osborn, R., Orbital and Spin Chains in ZnV2O4, Phys. Rev. Lett., 93, 156407/1-156407/4, 2004.

[11]. Ebbinghaus, S. G., Hanss, J., Klemmb, M. and Horn, S., Crystal structure and magnetic properties of ZnV_2O_4, Journal of Alloys and Compounds, 75–79, 370, 2004.

[12]. Zhang , Z., Louca, D., Visinoiu, A. and Lee ,S.-H., Local order and frustration in the geometrically frustrated spinels $Cd_{1-x}Zn_xV_2O_4$, Phys. Rev. B, 74, 014108/1-014108/9, 2006.

[13]. Takubo, K., Son , J.-Y., Mizokawa, T., Ueda ,H., Isobe, M., Matsushita, Y. and Ueda, Y., Electronic structure of AV_2O_4 (A =Li, Zn, and Cd) studied by x-ray photoemission spectroscopy, Phys. Rev. B, 74, 155103/1-155103/5, 2006.

[14]. Vasilieva , A. N., Markinaa, M. M., , Isobeb, M., Ueda, Y., Specific heat and magnetic susceptibility of spinel compounds CdV_2O_4, ZnV_2O_4 and $MgTi_2O_4$, Journal of Magnetism and Magnetic Materials , e375 –e377,300, 2006.

[15]. Kuntscher, C., Rabia, K. , Forthaus, M. K. , Abd-Elmeguid, M. M. , Rivadulla, F., Kato, Y. and Batista, C. D., Nonmonotonic evolution of the charge gap in ZnV_2O_4 under pressure, Phys. Rev. B 86, 020405/1-020405 /5(R), 2012.

[16]. Plumier, R. and Sougi, M., Observation of a first order transition in the ferrimagnetic spinel MnV_2O_4, Solid State Commun., 64, 53-55, 1987.

[17]. Plumier, R. and Sougi, M., Observation of a first-order transition at $T < T_c$ in MnV_2O_4, Physica B, 155, 315-319, 1989.

[18]. Adachi, K., Suzuki, T., Kato, K., Osaka, V., Takata, M. and Katsufuji, T., Magnetic-Field Switching of Crystal Structure in an Orbital-Spin-Coupled System: MnV_2O_4, Phys. Rev. Lett., 95, 197202/1-197202/4, 2005.

[19]. Garlea, V. O., Jin, R., Mandrus, D., Roessli, B., Huang, Q., Miller, M., Schultz, A. J. and Nagler, S. E., Magnetic and Orbital Ordering in the Spinel MnV_2O_4, Phys. Rev. Lett., 100, 066404/1-066404/4, 2008.

[20]. Chung, J. H., Kim, J. H., Lee, S. H., Sato, T. J., Suzuki, T., Katsumura, M. and Katsufuji, T., Magnetic excitations and orbital physics in the ferrimagnetic spinels MnB_2O_4 (B=Mn, V), Phys. Rev. B, 77, 054412/1-054412/5, 2008

[21]. Hardy, V., Bréard, Y. and Martin, C., Phase diagram of the spinel oxide MnV_2O_4, Phys. Rev. B, 78, 024406/1-024406/8, 2008

[22]. Pannunzio-Miner, E. V., De Paoli, J. M., Carbonio, R. E. and Sánchez, R. D., Nonadiabatic small polarons, positive magnetoresistance, and ferrimagnetism behavior in the partially inverse $Mn_{2-x}V_{1+x}O_4$ spinels, J. App. Phys., 105, 113906/1-113906/8, 2009.

[23]. Luo, X., Sun, Y. P., Hu, L., Wang, B. S., Lu, W. J., Zhu, X. B., Yang, Z. R. and Song, W. H., Observation of the large magnetocaloric effect in an orbital–spin-coupled system MnV_2O_4, J. Phys.: Condens. Matter, 21, 436010/1-436010/5, 2009.

[24]. Luo, X. , Sun, Y. P., Lu, W. J., Zhu, X. B., Yang, Z. R. and Song, W. H., Observation of the large orbital entropy in Zn-doped orbital-spin-coupled system MnV_2O_4, Appl. Phys. Lett., 96, 062506/1-062506/1, 2010.

[25]. Huang, Z. H., Luo, X., Hu, L., Tan, S. G., Liu, Y., Yuan, B., Chen, J. , Song, W. H. and Sun, Y. P., Observation of the large magnetocaloric effect and suppression of orbital entropy change in Fe-doped MnV_2O_4, J. Appl. Phys.,115, 034903/1-034903/5, 2014.

[26]. Kiswandhi, A., Brooks, J. S., Lu, J., Whalen, J., Siegrist, T. and Zhou, H. D., Chemical pressure effects on structural, magnetic, and transport properties of $Mn_{1-x}Co_xV_2O_4$, Phys. Rev. B, 84, 205138/1-205138/10, 2011.

[27]. Blanco-Canosa, S., Rivadulla, F., Pardo, V., Baldomir, D., Zhou, J. S., García-Hernández, M., López-Quintela, M. A., Rivas, J. and Goodenough, J. B., Enhanced Pressure Dependence of Magnetic Exchange in AV_2O_4 Spinels Approaching the Itinerant Electron Limit, Phys. Rev. Lett., 99, 187201, 2007.

[28]. Tanaka, M., Tokoro, T. and Aiyama, Y., Jahn-Teller Effects on Mössbauer Spectra of Fe_{57} in $FeCr_2O_4$ and FeV_2O_4, J. Phys. Soc. Jpn. 21, 262-267, 1966.

[29]. Katsufuji, T., Suzuki, T., Takei, H. and Shingu, M., KATO, K., OSAKA, K., TAKATA, M., SAGAYAMA, H. and ARIMA, T., Structural and Magnetic Properties of Spinel FeV_2O_4 with Two Ions Having Orbital Degrees of Freedom, J. Phys. Soc. Jpn., 77, 053708/1- 053708/4, 2008.

[30]. Nishihara, S., Doi, W., Ishibashi, H., Hosokoshi, Y., Ren, X.-M. and Mori, S., Appearance of magnetization jumps in magnetic hysteresis curves in spinel oxide FeV_2O_4, J. App. Phys., 107, 09A504/1-09A504/3, 2010.

[31]. MacDougall, G. J., Garlea, V. O., Aczel, A. A., Zhou, H. D. and Nagler, S. E., Magnetic order and ice rules in the multiferroic spinel FeV_2O_4, Phys. Rev. B, 86, 060414/1-060414/1(R), 2012.

[32]. Kang, J.-S., Hwang, J., Kim, D. H., Lee, E., Kim , W. C., Kim, C. S., Kwon, S., Lee, S., Kim, J.-Y., Ueno, T., Sawada, M., Kim, B., Kim, B. H., Min, B. I., Kim, B., Kim, B. H. and Min , B. I., Phys. Rev. B, 86, 125142/1-125142/8 , 2012.

[33]. Nii, Y., Sagayama, H., Arima, T., Aoyagi, S., Sakai, R., Maki, S., Nishibori, E., Sawa, H., Sugimoto, K., Ohsumi, H. and Takata, M., Orbital structures in spinel vanadates AV_2O_4 (A = Fe, Mn), Phys. Rev. B, 86, 125142/1-125142/8, 2012.

[34]. Zhang, Q., Singh, K., Guillou, F., Simon, C., Breard, Y., Caignaert, V., and Hardy, V., Ordering process and ferroelectricity in a spinel derived from FeV_2O_4, Phys. Rev. B, 85, 054405/1-054405/10, 2012.

[35]. Liu, N., Zhao, K. H., Shi, X. L. and Zhang, L. W., Fe3+ doping effects on the structure and multiferroicity of $Fe_{1+x}V_{2-x}O4$ ($0 \leq x \leq 0.4$) spinels, J. Appl. Phys., 111, 124112/1-124112/5, 2012.

[36]. Rogers, D. B., Arnott, R. J., Wold, A. and Goodenough, J. B., The preparation and properties of some vanadium spinels, J. Phys. Chem. Solids, 24, 347-360, 1963.

[37]. Menyuk, N., Wold, A., Rogers, D. and Dwight, K., Magnetic Transitions in Cubic Spinels, J. Appl. Phys. 33, 1144-1145, 1962.

[38]. Sawaoka, A., Miyahara, S., Nagasaki, H. and Minomura, S., Effect of pressure on the electrical resistivity of some vanadium spinels, Solid State Commun., 3, 155-158, 1965.

[39]. Tejada, J., Oliva, M. and Rodriguez, R., After effects of orbital electron capture in Co spinels, Solid State Commun., 30, 645-650, 1979.

[40]. Lyons, D. H., Kaplan, T. A., Dwight, K. and Menyuk, N., Classical Theory of the Ground Spin-State in Cubic Spinels, Phys. Rev., 126, 540-555, 1962.

[41]. Dwight, K., Menyuk, N., Rogers, D. B. and Wold, A., Proc. Int. Conf. on Magnetism 1964-65 (Nottingham).

[42]. Kismarahardja, A., Brooks, J. S., Kiswandhi, A., Matsubayashi, K., Yamanaka, R., Uwatoko, Y., Whalen, J., Siegrist, T. and Zhou, H. D., $Co[V_2]O_4$: A Spinel Approaching the Itinerant Electron Limit, Phys. Rev. Lett., 106, 056602/1-056602/4, 2011.

[43]. Huang, Y., Yang, Z. and Zhang, Y., Magnetic, structural, and thermal properties of CoV_2O_4, J. Phys. Condens. Matter, 24, 056003/1- 056003/5, 2012.

[44]. Huang, Y., Pi, L., Tan, S., Yang, Z. and Zhang, Y., Formation and partial melting of two types of spin-cluster glass behavior in vanadate spinel, J. Phys. Condens. Matter, 24, 056001/1-056001/5, 2012.

[45]. Lancashire, R. J., CHEM1902 (C10K) Coordination Chemistry, An Introductory Course at UWI, Jamaica. 2010.

[46]. Dunitz, J. D. and Orgel, L. E., Electronic properties of transition-metal oxides-II: Cation distribution amongst octahedral and tetrahedral sites, J. Phys. Chem. Solids, 3, 318-323, 1957.

[47]. Ballhausen, C. J. and Dan, J., Theory of Copper (II)-Spectra, Mat. Fys. Medd., 29,4. 1954.

[48]. Cotton, F. A., Chemical Applications of Group Theory, Wiley, New York, 1990.

[49]. Cox, P. A., Transition Metal Oxides, Oxford University Press, New York, 1992.

[50]. Jahn, H. A. and Teller, E., Stability of polyatomic molecules in degenerate electronic states. I. Orbital degeneracy, Proc. R. Soc. Lond. A, 161, 220-235,1937.

[51]. Senn, P., A simple quantum mechanical model that illustrates the Jahn-Teller effect, J. Chem. Educ., 69, 819-821, 1992.

[52]. Asher, E., Rieder, H., Schmid, H. and Stossel, H., Some Properties of Ferromagnetoelectric Nickel-Iodine Boracite, $Ni_3B_7O_{13}$ I, J. Appl. Phys., 37, 1404-1405, 1966.

[53]. Spaldin, N. A., Magnetic Materials: Fundamentals and Applications, Cambridge University Press, New York, 2003.

[54]. Kaplan, T. A., Classical Spin-Configuration Stability in the Presence of Competing Exchange Forces, Phys. Rev., 116, 888-889, 1959.

[55]. Ramirez, A. P., Handbook of Magnetic Materials, edited by K. J. H. Busch, Elsevier Science, Amsterdam, 2001.

[56]. Nori, F. and Tonomura, A., Helical Spin Order on the Move, Science, 311, 344-345, 2006.

[57]. Prince, E., Crystal and magnetic structure of copper chromite, Acta Crystallogr, 10, 554-556, 1957.

[58]. Lee, S- H., Takagi, H., Louca, D., Matsuda, M., Ji, S., Ueda, H., Ueda, Y., Katsufuji, T., Chung, J-H., Park, S., Cheong, S-W. and Broholm, C., Frustrated Magnetism and Cooperative Phase Transitions in Spinels, J. Phys. Soc. Jpn., 79, 011004-0110017, 2010.

[59]. Smit, J. and Wijn, H. P. J., Ferrites, Wiley, New York, 1959.

[60]. Chikazumi, S., Physics of Ferromagnetism, Oxford University Press, Oxford, 2009.

[61]. Goodenough, J. B., Magnetism and the Chemical Bond, Krieger, New York, 1976.

[62]. Warburg, E., Magnetische untersuchungen, Ann. Phys (Leipzig), 13, 141-164, 1881.

[63]. P. Debye, Einige Bemerkungen Zur Magnetisierung bei tiefer tempratur, Ann. Phys. 81, 1154-1160, 1926.

[64]. Giauque, W. F., A thermodynamic treatment of certain magnetic effects. a proposed method of producing temperatures considerably below 1° absolute, J. Amer. Chem. Soc., 49, 1864-1870, 1927.

[65]. Pecharsky, V. K. and K. A. Gschneidner, Jr., Magnetic refrigeration materials, J. Appl. Phys., 85, 5365-5368, 1999.

[66]. Gschneidner Jr., K. A. and Pecharsky, V. K., Magnetocaloric materials, Annu. Rev. Mater. Sci. 30, 387-429, 2000.

[67]. Pecharsky, V. K. and Gschneidner Jr., K. A., Magnetocaloric effect and magnetic refrigeration, J. Magn. Magn. Mater., 200, 44-56, 1999.

[68]. Morrish, A. H., The Physical Principles of Magnetism, Wiley, New York, 1965.

[69]. Mott, N. F., Conduction in non-crystalline materials, Phil. Mag., 19, 835-852, 1969.

[70]. Lee, P. A. and Ramakrishnan, T. V., Reviews of Modern Physics, 57, 287-337, 1985.

[71]. Arrott, A., Criterion for Ferromagnetism from Observations of Magnetic Isotherms, Phys. Rev., 108, 1394-1396, 1957.

[72]. Arrott, A. and Noakes, J. E., Approximate Equation of State For Nickel Near its Critical Temperature, Phys. Rev. Lett., 19, 786-789, 1967.